Energy & Environmental Science

ROYAL SOCIETY OF CHEMISTRY

PAPER

View Article Online
View Journal | View Issue

Cite this: *Energy Environ. Sci.*, 2020, **13**, 5165

Unveiling the phonon scattering mechanisms in half-Heusler thermoelectric compounds†

Ran He,‡*[a] Taishan Zhu,‡[b] Yumei Wang,[c] Ulrike Wolff,[a] Jean-Christophe Jaud,[d] Andrei Sotnikov,[a] Pavel Potapov,[a] Daniel Wolf,[a] Pingjun Ying,[a] Max Wood,[e] Zhenhui Liu,[af] Le Feng,[af] Nicolas Perez Rodriguez,[a] G. Jeffrey Snyder,[e] Jeffrey C. Grossman,[b] Kornelius Nielsch*[afg] and Gabi Schierning*[a]

Received 7th June 2020,
Accepted 3rd November 2020

DOI: 10.1039/d0ee03014g

rsc.li/ees

Half-Heusler (HH) compounds are among the most promising thermoelectric (TE) materials for large-scale applications due to their superior properties such as high power factor, excellent mechanical and thermal reliability, and non-toxicity. Their only drawback is the remaining-high lattice thermal conductivity. Various mechanisms were reported with claimed effectiveness to enhance the phonon scattering of HH compounds including grain-boundary scattering, phase separation, and electron–phonon interaction. In this work, however, we show that point-defect scattering has been the dominant mechanism for phonon scattering other than the intrinsic phonon–phonon interaction for ZrCoSb and possibly many other HH compounds. Induced by the charge-compensation effect, the formation of Co/4d Frenkel point defects is responsible for the drastic reduction of lattice thermal conductivity in $ZrCoSb_{1-x}Sn_x$. Our work systematically depicts the phonon scattering profile of HH compounds and illuminates subsequent material optimizations.

Broader context

Solid-state thermoelectric technology has attracted great research interest in recent years for potential applications in thermal management and power generation. Enhancing the phonon scattering has been one of the most widely studied strategies to advance the thermoelectric materials' figure-of-merit (zT) as it avoids the complications in optimizing the intertwined electronic transport properties. This is particularly essential for certain thermoelectric materials such as half-Heusler compounds due to their intrinsic high lattice thermal conductivity. To date, the lattice thermal conductivity of optimized half-Heusler compounds remains well above the amorphous limit, thus meriting the importance of unveiling their phonon-transport features as well as the individual contributing mechanisms in scattering phonon. Herein, we show that point-defect scattering has been the major effective mechanism for phonon scattering other than the intrinsic phonon–phonon interaction for ZrCoSb and possibly other HH compounds. Furthermore, through a combination of experimental and first-principle approaches, we reveal that the intensified point-defect phonon scattering originates from the formation of Co/4d Frenkel-pair defects as a result of charge-compensation effects. This work advances the understanding of phonon transport properties in half-Heusler compounds, and thus provides a guideline for subsequently improving their thermoelectric properties.

[a] *Leibniz Institute for Solid State and Materials Research, Dresden, 01069, Germany. E-mail: r.he@ifw-dresden.de, k.nielsch@ifw-dresden.de, g.schierning@ifw-dresden.de*
[b] *Department of Materials Science and Engineering, Massachusetts Institute of Technology, Cambridge, MA 02139, USA*
[c] *Institute of Physics, Chinese Academy of Sciences, Beijing 100190, China*
[d] *Department of Materials and Earth Sciences, Technical University of Darmstadt, Darmstadt, 64287, Germany*
[e] *Department of Materials Science and Engineering, Northwestern University, Evanston, Illinois 60208, USA*
[f] *Institute of Materials Science, Technical University of Dresden, Dresden, 01062, Germany*
[g] *Institute of Applied Physics, Technical University of Dresden, Dresden, 01062, Germany*

† Electronic supplementary information (ESI) available. See DOI: 10.1039/d0ee03014g

‡ Equal contributors.

1. Introduction

By interconverting between heat and electricity, thermoelectric (TE) technology is potentially applicable under special scenarios such as active cooling[1] or powering the nodes of the internet of things (IoT).[2] In comparison to other competing technologies, TE devices perform reliably due to their solid-state nature. They are noise-free, maintenance-free, and emission-free. However, the current application of TE technology is restricted only within niche fields where reliability outweighs conversion efficiency. The large-scale application potential of TE technology is greatly hindered by the limited material properties, therefore, it is vitally important to improve the performance of TE materials.[3]

The performance of a TE material is characterized by its figure-of-merit (zT), $zT = \frac{S^2\sigma}{\kappa_{tot}}T$, where S, σ, T, and κ_{tot} are the Seebeck coefficient, the electrical conductivity, the absolute temperature, and the total thermal conductivity, respectively. In general, higher zT corresponds to better material performance. The term $S^2\sigma$ is the power factor. κ_{tot} has contributions from both the electronic (κ_e) and the lattice (κ_L) parts, *i.e.*, $\kappa_{tot} = \kappa_e + \kappa_L$. Among the various TE materials, the half-Heusler compounds are particularly promising for applications due to their decent higher-temperatures zT together with other advantages such as mechanical and thermal robustness, non-toxicity, and employment of low-cost and earth-abundant elements,[4–13] *etc.* Nevertheless, the zT values of half-Heusler compounds are relatively low when compared to some other TE materials such as Bi_2Te_3 or SnSe due to their remaining high thermal conductivity, especially the lattice contribution (κ_L).[14,15]

To reduce the κ_L of half-Heusler compounds, great efforts were undertaken, multiple strategies were proposed, and their performances in κ_L reduction were claimed. Fig. 1 summarizes the schematics of common mechanisms for phonon scattering. For example, Rausch *et al.* synthesized MCoSb half-Heusler compounds (M = Hf, Zr, Ti) through arc melting and ampoule annealing.[16] The final products possessed a phase-separation microstructure, which was used as an explanation for the reduction of κ_L. Yan *et al.* powderized half-Heusler ingots $MCoSb_{0.8}Sn_{0.2}$ (M is a combination among Hf, Zr, Ti) by high energy ball milling to reduce the grain size, and then applied a rapid sintering process using a current assisted hot pressing.[17] In comparison to the ingots that were synthesized through direct melting, the sintered products showed a significant reduction of κ_L by 30–40%, which was believed originated from the reduced grain size to ~200 nm.[17] Besides, several studies analyzed the phonon scattering mechanisms of NbFeSb- and ZrNiSn-based compounds and declared the considerable impact of electron–phonon scattering for the reduction of κ_L.[6,18,19]

The previous reports are heuristic in revealing the potential of intensified phonon scattering in optimizing the TE figure-of-merit. However, more elaborate investigations are needed to systematically depict the phonon scattering profiles such as quantitative analysis as well as controlled experiments. These criteria were not fully met by some of the usual investigating approaches. For example, the role of electron–phonon (EP) interaction for κ_L reduction was usually studied under the framework of the Debye model through simply asserting a scattering rate $\tau_{EP}^{-1} = C\omega^{\delta}$, where ω is the phonon frequency, C is a fitting parameter which was treated either as a constant[20] or carrier-concentration dependent.[18] Besides, the power-law dependence, δ, could be 1 or 2 if the derivations of Ziman[21] or Pippard[22] were employed, respectively. Although these flexibilities are convenient for analyzing the individual scattering mechanisms and fitting the ultimate κ_L, they inevitably obscure the essential physics and potentially yield incomplete or even flawed conclusions. In another example, κ_L reduction was obtained in MCoSb-based (M = Hf, Zr, Ti) compounds with a refined grain size of ~200 nm.[17] However, the study of phonon scattering from grain boundaries was qualitative. It remains unclear how the variation of grain size quantitatively influences phonon transport. Therefore, it is imperative to scrutinize the individual scattering sources and clarify their real contributions to the κ_L reduction.

Herein, to identify the major phonon-scattering mechanisms in half-Heusler compounds, we start from synthesizing ZrCoSb-based half-Heusler compounds with partial substitution of Sn at the Sb sites. Despite the small contrast of mass between Sb and Sn (121.76 *vs.* 118.71 u.a.m.), we observe a drastic κ_L reduction with increased Sn concentration. To understand the phonon-transport anomalies, we dissociate the individual mechanisms and investigate their contributions in scattering phonons through combined experimental and theoretical approaches. Our analyses show that the drastic κ_L reduction by increasing Sn cannot originate from an enhanced phonon–phonon interaction, phase boundary scattering, grain boundary scattering, or electron–phonon interaction. Furthermore, we comprehensively investigate the atomic-level defects through microstructural characterization and Rietveld refinement. We confirm the presence of Co/4d Frenkel-type defects, (*i.e.*, a simultaneous formation of Co vacancy and Co interstitials, as shown in Fig. 1) in the Sn-containing compounds, but not in the Sn-free compounds, which suggests that the substitution of Sn at the Sb sites essentially alters the point-defect features in the compounds. The formation of defects is electron-driven because of the charge-compensation effects,

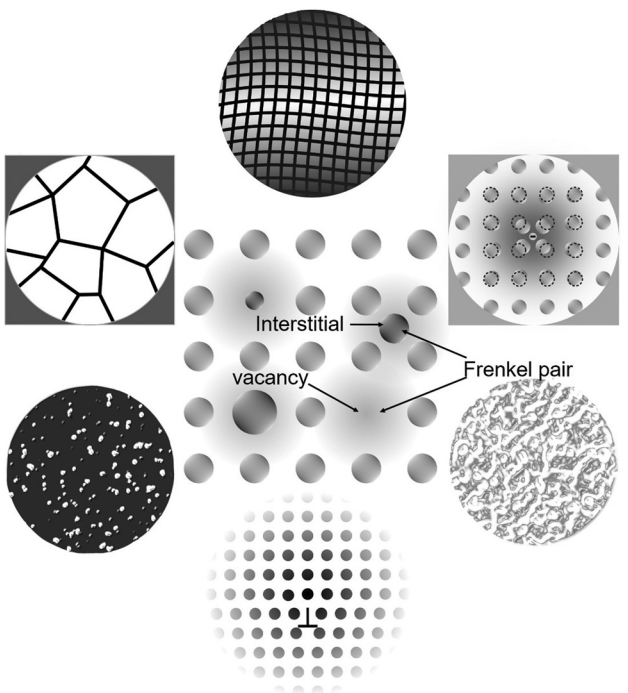

Fig. 1 Schematics of common phonon scattering mechanisms. Center: point defects. Surroundings (clockwise from the top middle): phonon–phonon interaction, electron–phonon interaction, phase separation, dislocations, decorative impurities, and grain boundaries. The Frenkel point defect is highlighted based on the conclusions of this work.

as indicated by the first-principle calculations. Furthermore, we evaluate the defect concentrations based on the BvK–Debye model. The calculated defect concentrations are consistent with the refinement results, thus further supporting the dominant role of Co/4d Frenkel point defects in phonon scattering for the ZrCoSb-based half-Heusler compounds. Besides, although our analyses are based on ZrCoSb, we show the extendibility of our conclusions to other half-Heusler compounds such as ZrNiSn, NbFeSb, and ZrCoBi, *etc.* due to their similar phonon scattering behaviors. This work advances the understanding of phonon transport in half-Heusler compounds by illuminating the phonon scattering profile, and thus provides a guideline for subsequent property optimization to enable a large-scale application of half-Heusler thermoelectric materials.

2 Results and discussion

2.1 Anomalous κ_L reduction of $ZrCoSb_{1-x}Sn_x$

We show in Fig. 2a the temperature-dependent κ_L of $ZrCoSb_{1-x}Sn_x$ from 300 K up to 973 K. The full thermoelectric (TE) properties can be found in the ESI† (Fig. S1 and S2). Notably, the substitution of Sn at the Sb sites yields a remarkable κ_L reduction. For example, the value of κ_L is ~20 W m^{-1} K^{-1} at 300 K for the pristine ZrCoSb, while it drops to ~4.4 W m^{-1} K^{-1} with 30% Sn substitution, showing an ~80% reduction. Such a huge κ_L reduction cannot originate from the minor differences of mass and radius between Sb and Sn. Besides, Fig. 2b compares the κ_L at 300 K and 973 K between the two series of compounds: $ZrCoSb_{1-x}Sn_x$ and $Zr_{1-y}Ti_yCoSb$. We find that the Sn-substituted compounds have an even larger κ_L reduction than the ones with Ti substitution. Considering that the mass difference between Sn and Sb is only 3% (118.71 *vs.* 121.76 u.a.m.), much smaller than the 48% between Ti and Zr (47.867 *vs.* 91.224 u.a.m.), our results disobey the common rule that larger differences of atomic mass and radius yield stronger phonon scattering. Similar phonon transport anomalies were also reported in other half-Heusler compounds including n-type Zr(Co,Ni)Sb,[23] n-type NbCo(Sn,Sb),[24] p-type (Nb,Zr)FeSb,[6] p-type Ti(Co,Fe)Sb,[25] and p-type Zr(Co,Fe)Sb (this work, see below), *etc.*, as summarized in the ESI† (Fig. S3). In the following paragraphs, we aim at elucidating these κ_L anomalies in half-Heusler compounds by scrutinizing the individual phonon scattering mechanisms and discussing their contributions for the reduction of κ_L.

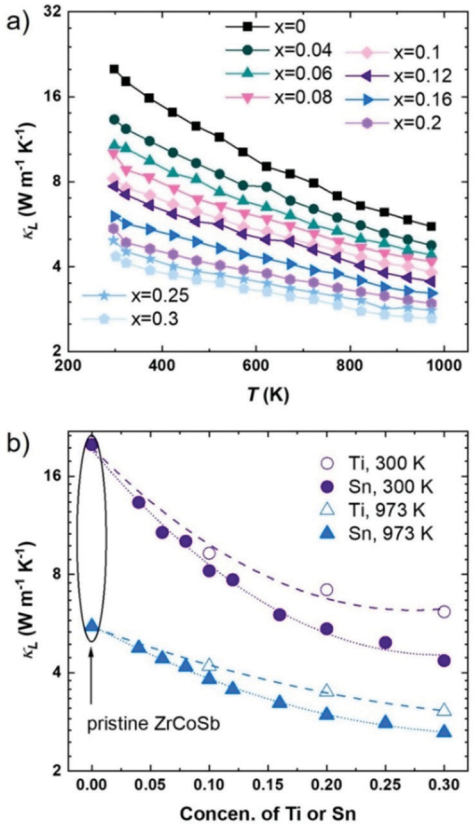

Fig. 2 (a) Temperature-dependent lattice thermal conductivity of $ZrCoSb_{1-x}Sn_x$. (b) Composition-dependent lattice thermal conductivity of $ZrCoSb_{1-x}Sn_x$ and $Zr_{1-y}Ti_yCoSb$ at 300 K and 973 K, where x = 0, 0.04, 0.06, 0.08, 0.1, 0.12, 0.16, 0.2, 0.25, and 0.3; y = 0, 0.1, 0.2, and 0.3. The dashed and dotted lines in (b) are for eye guidance.

2.2 Uncovering the phonon scattering mechanisms for κ_L reduction

2.2.1 Three-phonon process. Usually, the intrinsic phonon–phonon interaction (three-phonon process) dominates the scattering of phonons at high temperatures, and $\kappa_L = \frac{(6\pi^2)^{2/3}\bar{M}}{V^{2/3}4\pi^2\gamma^2 T}v_g^3$, where $\bar{M}$ is the average atomic mass, V is the atomic volume, γ is the Grüneisen parameter, and v_g is the average group velocity.[26] The substitution of Sn at the Sb sites changes the chemical composition and potentially alters the bonding characteristics inside the lattice. This can yield variations in v_g and γ, which might subsequently modify the intensity of the three-phonon process.[27] Typically, v_g can be adequately represented by the average speed of sound (v_A). Therefore, κ_L can be potentially suppressed if v_A is reduced. This mechanism was demonstrated to significantly reduce the κ_L of the ZrCoBi-based compounds.[7]

To examine the relevance of this mechanism for $ZrCoSb_{1-x}Sn_x$, we measure the sound speed of the shear (v_S) and longitudinal (v_L) modes for the compounds $ZrCoSb_{1-x}Sn_x$ and $Zr_{1-y}Ti_yCoSb$ at 300 K, and calculate the v_A through $\frac{1}{v_A^3} = \frac{1}{3}\left(\frac{1}{v_L^3}+\frac{2}{v_S^3}\right)$. The measurement details can be found in the ESI.† As shown in Fig. 3a, a slight v_A reduction of ~5% is realized with an increased concentration of Sn from 0 to 0.3. This is consistent with our first-principles calculations in Fig. S4 (ESI†), where v_g is shown for individual modes and the difference between 0% and 12.5% Sn substitutions is within 5%. Due to the $\kappa_L \propto v_g^3$ relation, the reduction of κ_L cannot exceed ~15% solely by sound-speed suppression. This is much less than the 80% κ_L reduction at 300 K that is experimentally observed. Moreover, we evaluate the mode-dependent Grüneisen

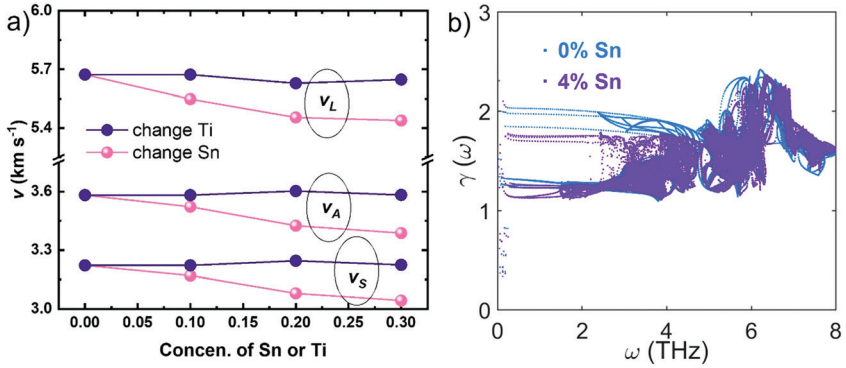

Fig. 3 (a) Longitudinal-mode (v_L), shear-mode (v_S), and average (v_A) speed of sound of $ZrCoSb_{1-x}Sn_x$ and $Zr_{1-y}Ti_yCoSb$, where x and y = 0, 0.1, 0.2, and 0.3. (b) Mode-dependent Grüneisen parameter of ZrCoSb upon 0% and 4% Sn-substitution.

parameter (γ) of ZrCoSb with 0% and 4% Sn substitution through the first-principle calculation. As shown in Fig. 3b, increasing the concentration of Sn yields a reduction of γ, especially for the acoustic branches that carry most heat. The reduction of γ indicates a less anharmonic lattice vibration upon substituting Sn at the Sb sites. Note that the reduction in γ^2 is also roughly ~15%, which is similar to the reduction of $v_A{}^3$. Accordingly, the phonon–phonon interaction should yield limited perturbation to κ_L for the compound series $ZrCoSb_{1-x}Sn_x$. Therefore, to realize the drastic κ_L reduction of $ZrCoSb_{1-x}Sn_x$, a different phonon scattering origin must present which escalates with the increase of x.

To additionally assess the impact from the three-phonon process in ZrCoSb upon the substitution of Sn, we calculated the phonon dispersion relations for two compounds, ZrCoSb and $ZrCoSb_{0.875}Sn_{0.125}$ (if one Sb atom is replaced by Sn). The calculation details as well as the phonon-transport parameters such as phonon dispersions, scattering rates, and group velocities are discussed in the ESI† (Fig. S4). We find that the composition-dependent variation trend of κ_L from experiments differs obviously from its calculation counterparts (Fig. S5, ESI†), thus further supporting a major phonon scattering from another mechanism in the Sn-added compounds.

2.2.2 Impurity scattering. One common strategy to reduce the κ_L of TE materials is to include secondary phases. Such structures are formed either by embedding decorative impurities into the half-Heusler matrix including full-Heusler, pure elements, and oxides, *etc.*;[28,29] or by decomposing the nominal composition into several regions with elemental segregation but maintaining the half-Heusler structure, *i.e.*, the phase-separation strategy. For example, the phase-separated $ZrCoSb_{0.8}Sn_{0.2}$ possesses one Sb-rich phase ($Zr_{1.02}Co_{0.96}Sb_{0.87}Sn_{0.16}$) and one Sn-rich phase ($Zr_{1.01}Co_{0.96}Sb_{0.15}Sn_{0.88}$).[16] This structure was believed to be effective in scattering phonon and reducing the κ_L. Following this concept, we examine the phase purity for the compounds synthesized in this work. As shown in the ESI† (Fig. S6), the XRD patterns of all compounds within the $ZrCoSb_{1-x}Sn_x$ series can be indexed as single-phase half-Heuslers with no observable impurity peaks. Also, the elemental mappings of $ZrCoSb_{0.8}Sn_{0.2}$ are characterized by SEM-EDX and displayed in Fig. S7 (ESI†). No elemental segregation can be observed for the $ZrCoSb_{1-x}Sn_x$ compound series synthesized in this work under the spatial resolution limit of SEM-EDX mapping (~1 μm), indicating an improved purity in this work.

Moreover, we show that the impurity species of ZrCoSb-based half-Heusler compounds highly depend on the synthesis routines as well as the initial stoichiometry of the compounds. For comparison, we specifically prepare another $ZrCoSb_{0.8}Sn_{0.2}$ using a different approach that generates impurities including elemental Zr and an unknown phase that is rich in Co and Sn. The details of sample synthesis, as well as the corresponding elemental mapping, can be found in the ESI† (Section I and Fig. S7). Together with two more samples from previous reports,[16,30] the distinct impurity features are listed in Table 1 of several specimens with almost identical composition $ZrCoSb_{0.8}Sn_{0.2}$. Subsequently, we compare the thermal conductivities among these specimens. As shown in Fig. 4, the thermal conductivities almost overlap from room temperature up to 973 K among these specimens regardless of the impurity details. This indicates that the major phonon scattering mechanism should be independent of the diversified impurity characteristics. Therefore, phonon scattering from decorative secondary phases is not considered dominant for half-Heusler $ZrCoSb_{1-x}Sn_x$ because comparable κ_L reduction is attainable for single-phase compounds with improved uniformity in elemental distribution.

Table 1 The impurity features of $ZrCoSb_{0.8}Sn_{0.2}$ compounds under different synthesis conditions

Label	Synthesis conditions	SEM-EDX impurities	Ref.
A	arc melting + sintering; with extra (3 to 7%) Co	Full-Heusler	30
B	arc melting + ampoule annealing	Phase separation	16
C	arc melting + short-term (2 h) ball milling + sintering	Zr + (Co,Sn)-rich	This work
D	long-term (30 h) ball milling + sintering (1323 K for 3 minutes)	Not observable	This work
E	long-term (30 h) ball milling + sintering (1473 K for 30 minutes)	Not observable	This work

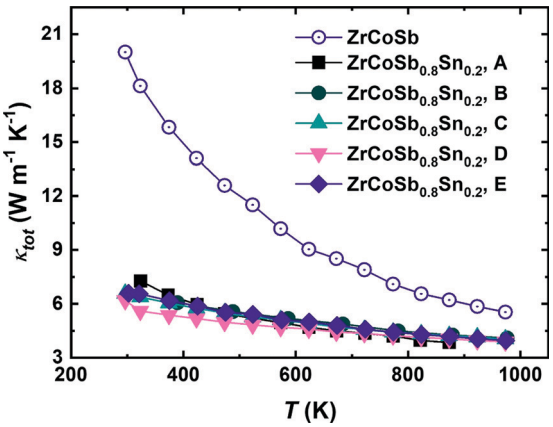

Fig. 4 The thermal conductivity of several $ZrCoSb_{0.8}Sn_{0.2}$ compounds with distinct impurity features, the sample labels (A–E) are following Table 1. For comparison, the thermal conductivity of ZrCoSb is also plotted.

Note that it is not possible to completely remove the impurities. However, the species and the quantity of the impurities are important in affecting the ultimate thermal conductivity. As respectively shown in Fig. S8 and S9 (ESI†), the TEM-EDX mappings on $ZrCoSb_{0.7}Sn_{0.3}$ and ZrCoSb display some sparsely distributed precipitates with lengths in the range of a few tens to a few hundreds of nanometers that are invisible by SEM-EDX, thus corroborating the improved purity when compared to other synthesis approaches. These impurities are rich mostly in Sn, Zr, and Sb. Therefore, these precipitates are unlikely to significantly reduce the κ considering their low concentration and the high thermal conductivity of Sn ($\sim$60 W m^{-1} K^{-1}), Zr ($\sim$20 W m^{-1} K^{-1}), and Sb ($\sim$20 W m^{-1} K^{-1}) at room temperature.

2.2.3 Grain boundary scattering. Nanostructure is considered one of the most successful strategies for improving the TE performance by greatly impeding the phonon transport yet leaving the electrons less perturbed. This concept was also employed extensively to explain the experimentally reduced κ_L in half-Heusler compounds. Generally, a refined grain size of $\sim$200 nm was claimed sufficient to decouple the transport of electron and phonon so that the overall thermoelectric performance can be significantly improved.[17,31–34] To analyze the effectiveness of grain boundary scattering in phonon transport, we show the SEM images of the freshly broken surfaces of ZrCoSb, $Zr_{0.7}Ti_{0.3}CoSb$, and $ZrCoSb_{0.7}Sn_{0.3}$ in Fig. 5a–c, respectively, and evaluate the statistic grain sizes in the ESI† (Fig. S10). We find that almost all grains of $ZrCoSb_{0.7}Sn_{0.3}$ are at the sub-micron level, with an area-weighted average grain size of $\sim$187 nm, as shown in Fig. S10 (ESI†). In contrast, the ZrCoSb and $Zr_{0.7}Ti_{0.3}CoSb$ possess grains that are much larger than $ZrCoSb_{0.7}Sn_{0.3}$ ($\sim$1251 nm and $\sim$799 nm, respectively). Similar results were also reported by Zhu *et al.* in the ZrCoBi-based half-Heusler compounds where the grains were greatly refined upon aliovalent doping.[7] The mechanisms for such distinct grain morphologies remain less investigated. We speculate that aliovalent doping modifies the powder properties such as electrical conductivity or melting temperature,

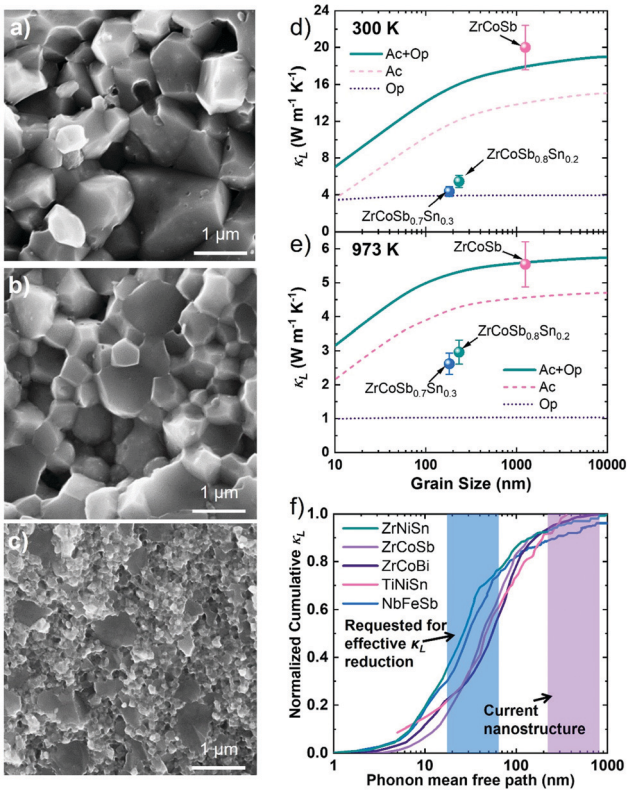

Fig. 5 SEM images of (a) ZrCoSb, (b) $Zr_{0.7}Ti_{0.3}CoSb$, and (c) $ZrCoSb_{0.7}Sn_{0.3}$. The experimental lattice thermal conductivity of ZrCoSb, $ZrCoSb_{0.8}Sn_{0.2}$, and $ZrCoSb_{0.7}Sn_{0.3}$ together with the calculated grain-size-dependent of ZrCoSb based on the BvK–Debye model at (d) 300 K and (e) 973 K. Contributions from the acoustic (Ac) and optical (Op) branches are individually presented. The error bars correspond to a 12% relative error in lattice thermal conductivity. (f) The normalized cumulative lattice thermal conductivity of NbFeSb,[37] ZrCoSb,[36] ZrCoBi,[7] TiNiSn,[38] and ZrNiSn[37] from first-principle calculations at 300 K. The purple color indicates the experimentally realized grain sizes of nanostructured half-Heusler compounds and the blue color suggests the desired sizes for effective phonon scattering.

which subsequently alter the grain-growth behaviors during the current-assisted sintering procedures.

Based on the SEM characterization results, it would be plausible to conclude a dominant phonon scattering by grain boundaries since smaller grain sizes are indeed obtained in compounds with a higher concentration of Sn. To verify this assertion, we modify the sintering condition for the composition $ZrCoSb_{0.8}Sn_{0.2}$ by applying a higher temperature (1473 K) with an extended holding time (30 min). The new sintering condition enlarges the average grain sizes by $\sim$3 times from $\sim$233 nm to $\sim$679 nm, as shown in Fig. S10 (ESI†). On the other hand, as shown in Table 1 and Fig. 4, the κ_L varies negligibly despite such a significant grain enlargement, suggesting that grain refinement down to $\sim$200 nm cannot significantly contribute to the reduction of κ_L in half-Heusler compounds ZrCoSb.

Furthermore, we evaluate κ_L under varied grain sizes by employing a frequency-dependent scattering rate (*i.e.*, non-grey model) within the framework of the BvK–Debye model. The details are presented in the ESI† (Section VIII). Herein, we consider the

two major scattering mechanisms: (1) the intrinsic phonon–phonon interaction, which dominates the reduction of κ_L at higher temperatures for grain-boundary-free compounds (*i.e.*, single crystals), and (2) the grain boundary scattering. For simplification, we do not consider the point defect scattering by the substitution at the Sb/Sn site due to their negligible differences in mass and radius. Our calculation suggests that, as shown in Fig. 5d and e, with the SEM-observed grain sizes, boundary scattering yields ~11% and ~5.5% κ_L reduction for ZrCoSb at 300 K and 973 K, respectively. Besides, the grain-size-dependent κ_L from acoustic (Ac) and optical (Op) branches are shown individually following the BvK–Debye model, suggesting that boundary scattering mainly impacts the acoustic branches. Besides, the BvK–Debye model suggests that the optical branches contribute ~20% to the κ_L. This result is consistent with previous first-principle calculations for a variety of materials such as nanocrystalline Si and half-Heusler ZrCoBi,[7,35] and thus justifying the reliability of the BvK–Debye model in analyzing phonon transport. On the other hand, to suppress the lattice thermal conductivity from ~20 W m^{-1} K^{-1} (of ZrCoSb) to ~4.4 W m^{-1} K^{-1} (of $ZrCoSb_{0.7}Sn_{0.3}$), grain sizes of ~10 nm would be demanded. The demanded grain size is 1 to 2 orders of magnitude smaller than the SEM-observed grain sizes. Such a large discrepancy strongly indicates that grain boundaries should not be accountable for the reduction of κ_L for ZrCoSb-based half-Heusler compounds.

Moreover, our conclusion is further supported by previous first-principle calculations. Fig. 5f summarizes the phonon-mean-free-path-dependent accumulative normalized κ_L of ZrCoSb,[36] NbFeSb,[37] ZrNiSn,[37] ZrCoBi,[7] and TiNiSn.[38] The purple- and blue-shaded regions represent the grain size of the current nanostructured bulk compounds and the required grain size for κ_L reduction by ~40% to 60% from grain boundary scattering alone, respectively. The grain size in the current nanostructured compounds is insufficient to yield significant κ_L reduction for these compounds, and the necessity of grain refinement down to the order of ~10 nm is again confirmed. Our analyses indicate the insignificant role of grain boundary scattering in phonon scattering of ZrCoSb-based and possibly some other half-Heusler compounds.

Note that our conclusion differs from the previous reports about the effects of nanostructure in κ_L reduction for half-Heusler compounds. We speculate this is because most of the previous work investigated compounds, such as $Zr_{0.5}Hf_{0.5}CoSb_{0.8}Sn_{0.2}$, that are highly alloyed,[17] whereas in this work such heavy alloying is absent. In the highly alloyed compounds, phonons with higher frequencies are severely scattered by point defects, thus enlarging the portion of the lower-frequency phonons in κ_L. Therefore, by subsequently applying nanostructure that mainly targets at lower-frequency phonons, a larger κ_L reduction may be achieved for a highly alloyed specimen. Our work indicates the necessity of additional investigations to further understand the role of boundary scatterings in the reduction of κ_L.

2.2.4 Electron–phonon interaction. As another possible mechanism, electron–phonon (EP) interaction is typically important for phonon scattering at low temperatures.[21] Nevertheless, it is also effective to reduce κ_L for some materials such as Si and SiGe alloys at room temperature, provided that the carrier concentration (n_H) is sufficiently high.[39–41] By doping Sn into ZrCoSb, the increased κ_L will potentially yield a stronger EP interaction and κ_L reduction. Fig. 6a shows a monotonic decreasing trend of κ_L *vs.* n_H for compounds $ZrCoSb_{1-x}Sn_x$. However, this simple correlation is inadequate to justify the role of EP interaction in κ_L reduction. To reveal the contribution of EP interaction in ZrCoSb for phonon scattering, we synthesize another series of compounds, $ZrCo_{1-z}Fe_zSb$ with z = 0, 0.06, 0.1, and 0.15 as the control group. Herein, we select Fe as the dopant to minimize the phonon scattering from other mechanisms such as mass fluctuation. As shown in Fig. 6a, we find that Fe is also a p-type dopant but with much less doping efficiency, yet it generates a κ_L reduction that is comparable to the Sn-containing compounds. For example, with 10% elemental substitution, the κ_L values of $ZrCoSb_{0.9}Sn_{0.1}$ and $ZrCo_{0.9}Fe_{0.1}Sb$ at 300 K are 8.2 W m^{-1} K^{-1} and 7.7 W m^{-1} K^{-1}, respectively, showing a ~6% difference which is within the measurement error. However, the carrier concentration of $ZrCoSb_{0.9}Sn_{0.1}$ is ~12.8 × 10^{20} cm^{-3}, meanwhile, for $ZrCo_{0.9}Fe_{0.1}Sb$ it is only ~3.3 × 10^{20} cm^{-3}, differs by ~400%. The huge discrepancy between the two variation trends of κ_L *vs.* n_H suggests that the electron–phonon scattering is unlikely to govern the reduction of κ_L for carrier concentration at the ~10^{21} cm^{-3} level. Besides, the insignificant effect of EP interaction in reducing the κ_L was also discussed in n-type ZrCoSb.[23] By contrast, Fig. 6b shows the relations of κ_L *vs.* dopant

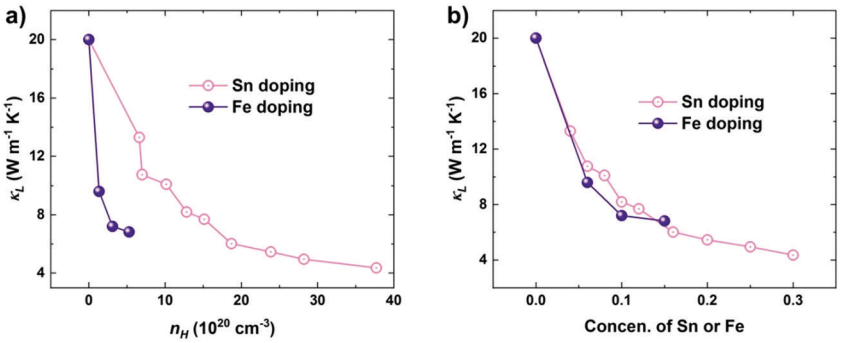

Fig. 6 The correlation of (a) κ_L *vs.* carrier concentration and (b) κ_L *vs.* dopant concentration for $ZrCoSb_{1-x}Sn_x$ and $ZrCo_{1-z}Fe_zSb$ at 300 K.

concentration (instead of carrier concentration) almost overlap between the two series of compounds, suggesting that the κ_L reduction has an atomic origin instead of an electronic one.

Additionally, we investigate the extendibility of our conclusion to other half-Heusler compounds including the NbFeSb and ZrCoBi. Upon parameterizing the scattering events, we show that the impacts of EP interaction on the κ_L in NbFeSb and ZrCoBi are weaker than that in ZrCoSb. A detailed analysis can be found in the ESI† (Section IX). Thus, the electron–phonon interaction cannot be a contributing mechanism for the experimentally observed κ_L reduction in ZrCoSb, NbFeSb, and ZrCoBi, and possibly other half-Heusler compounds such as ZrNiSn,[42] as recently reported by Ren *et al.*

2.2.5 Point defect scattering. With phonon–phonon interaction, phase boundary scattering, grain boundary scattering, and electron–phonon interaction being excluded, we now turn to point defects and show them to be the major contributor for phonon scattering. One important footprint of the phonon scattering mechanism is the variation index (α) for temperature ($\kappa_L \sim T^{\alpha}$), especially at well above the Debye temperature where all the vibration modes are adequately excited. Callaway and Klemens suggested -1 and -0.5 for α if the dominant scattering mechanisms are three-phonon process and point defect scattering, respectively.[43–45] Accordingly, we evaluate α based on the κ_L values within the range from 473 K to 773 K, which is above the Debye temperature ($\sim$400 K) of $ZrCoSb_{1-x}Sn_x$ so that phonon vibrations are fully activated, but also well below the intrinsic excitation temperature so that the bipolar thermal conductivity is negligible. As shown in Fig. 7, we obtain a gradual transition of α from -1 to -0.5 by increasing the concentration of Sn from 0 to 0.3, which indicates that the major scattering mechanism of phonons is shifted from phonon–phonon interaction to point defect scattering. Moreover, we evaluate α for several other compound series from previous reports including Zr(Co,Ni)Sb,[23] (Nb,Ti)FeSb,[18] (Nb,Zr)FeSb,[6] Ti(Co,Ni)Sb,[46] Ti(Co,Fe)Sb,[25] Zr(Co,Fe)Sb (this work), and (Zr,Ti)CoSb (this work). As shown in Fig. 7, similar variation trends are obtained for a variety of compounds, confirming the consistency regarding the transition of the major phonon scattering mechanism among these half-Heusler compounds. However, effective phonon scattering by point defects demands large differences in atomic mass and radius, yet replacing Sn at the Sb sites is inadequate. Therefore, we consider that another type of point defect must exist that can scatter phonons more effectively.

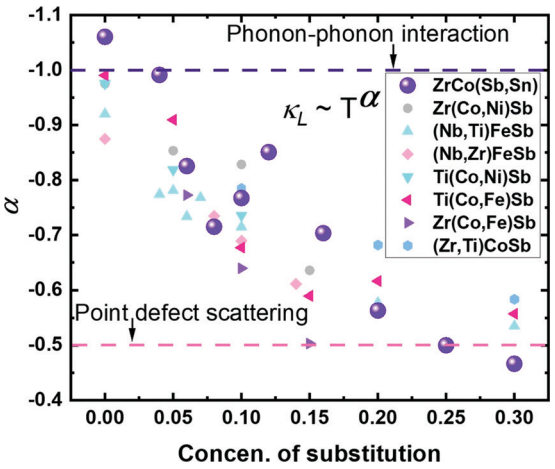

Fig. 7 Composition-dependent variation index (α) of $ZrCoSb_{1-x}Sn_x$, which is evaluated using κ_L values within the range from 573 K to 823 K. Other series of compounds are also included for comparison including Zr(Co,Ni)Sb,[23] (Nb,Ti)FeSb,[18] (Nb,Zr)FeSb,[6] Ti(Co,Ni)Sb,[46] Ti(Co,Fe)Sb,[25] Zr(Co,Fe)Sb (this work), and (Zr,Ti)CoSb (this work). The two horizontal lines individually indicate the values of α under the phonon–phonon interaction (-1) and the point defect scattering (-0.5).

2.3 Point defect details in the Sn-doped half-Heusler ZrCoSb

The half-Heusler compounds are crystalized with space group $F\bar{4}3M$. Ideally, the lattice is constituted by three interpenetrating fcc sublattices, and the remaining tetrahedral sites are unoccupied. Fig. 8a shows the structure model of half-Heusler ZrCoSb and full-Heusler $ZrCo_2Sb$. In full-Heusler $ZrCo_2Sb$, the Zr and Sb atoms occupy the Wyckoff positions 4b ($\frac{1}{2}$, $\frac{1}{2}$, $\frac{1}{2}$) and 4a (0, 0, 0), respectively, and the Co atoms occupy both the 4c ($\frac{1}{4}$, $\frac{1}{4}$, $\frac{1}{4}$) and 4d ($\frac{3}{4}$, $\frac{3}{4}$, $\frac{3}{4}$) positions; while in half-Heusler ZrCoSb, the 4d ($\frac{3}{4}$, $\frac{3}{4}$, $\frac{3}{4}$) sites are vacant. In reality, however, crystals are usually disordered naturally. One typical example is the ZrNiSn-based compounds where excess Ni, usually $\sim$5%, were repeatedly reported, yielding real compositions of $ZrNi_{1+\delta}Sn$.[47–51] The occupation status of the 4d sites can be examined by selected area electron diffraction (SAED). As shown in Fig. 8b, we simulate the [110] SAED patterns for half-Heusler ZrCoSb and full-Heusler $ZrCo_2Sb$. The two diffraction patterns are similar to each other, but the full-Heusler one has obvious alternating intensities from one reflection column to another along the [00l] direction, which is distinct from that of the half-Heusler compounds.

2.3.1 Defect analysis through STEM. Accordingly, we perform a TEM investigation to study the atomic-level defects. Fig. 8c displays a typical low-magnification TEM image of $ZrCoSb_{0.7}Sn_{0.3}$, from which we confirm the SEM-observed grain sizes of $\sim$200 nm. Moreover, we note that the material possesses great crystallinity with certain types of defects, such as dislocations, barely observable in the specimen, which indicates their minor contribution in phonon scattering. Additional low-magnification TEM images can be found in the ESI† (Fig. S12). The inset of Fig. 8c shows the SAED pattern with beam oriented along the [110] zone axis. Some extra reflections (as marked by yellow circles) appear in the pattern because the selected area might capture small regions from the neighboring grains with different orientations. Nevertheless, the SAED pattern can be indexed as Heusler structure with features of occupied 4d sites. Furthermore, we display in Fig. 8d and e the annular-bright-field (ABF) and high-angle annular-dark-field (HAADF) scanning transmission electron microscopy (STEM) images of $ZrCoSb_{0.7}Sn_{0.3}$, respectively. The images are taken along the [110] direction, from which the four lattice sites (4a, 4b, 4c, and 4d) do not overlap with each other so that the vacancy sites are visible. For better clarity, we magnify a selected region from

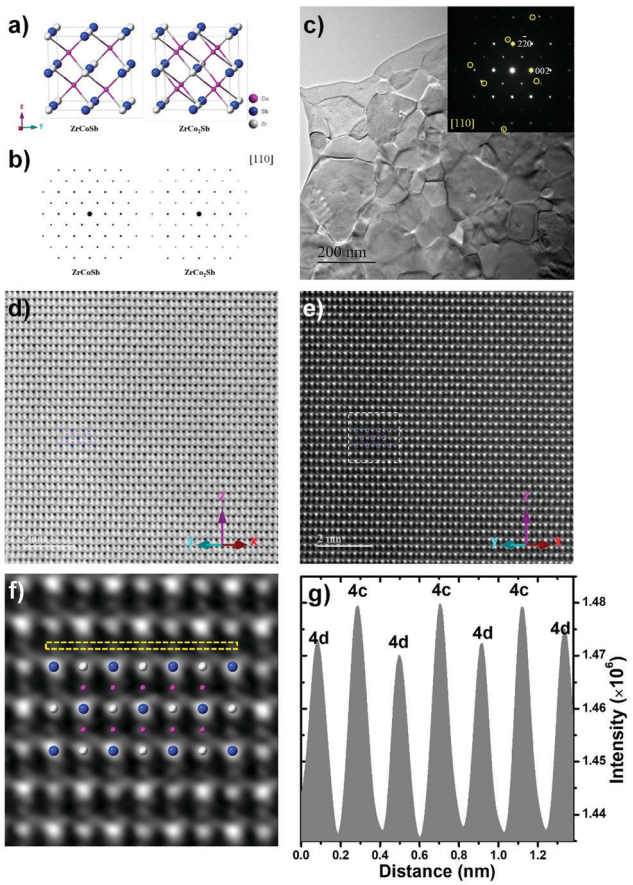

Fig. 8 (a) Lattice unit cells of half-Heusler ZrCoSb and full-Heusler $ZrCo_2Sb$. (b) The simulated electron diffraction patterns of ZrCoSb and $ZrCo_2Sb$ with beam orientation along the [110] zone-axis. (c) Low-magnification TEM image of $ZrCoSb_{0.7}Sn_{0.3}$, the inset is the indexed selected area electron diffraction (SAED) pattern in [110] zone-axis. (d) Annular-bright-field scanning transmission electron microscopy (ABF-STEM), and (e) high-angle annular-dark-field scanning transmission electron microscopy (HAADF-STEM) image of $ZrCoSb_{0.7}Sn_{0.3}$ [110] zone-axis. (f) The magnified HAADF-STEM image of (e), the crystal structure of full-Heusler is also inserted to show the occupation of both 4c and 4d positions. (g) The intensity profile is taken along the 4c/4d plane and integrated over the width of the atomic columns, as indicated by the yellow dashed box in (f). The alternating intensities suggest that the 4d sites are only partially occupied.

the HAADF-STEM image, as indicated by the white square in Fig. 8e. The magnified HAADF-STEM image is presented in Fig. 8f, from which the occupation of 4d lattice sites is observed. Moreover, we calculate in Fig. 8g the intensity profile (integrated over the width of the atomic columns) within the 4c/4d plane from the HAADF-STEM micrograph, as indicated by the yellow dashed box in Fig. 8f. Interestingly, an alternating intensity within the 4c/4d plane is observed, suggesting that the 4d sites are only partially occupied. It is widely known that vacancy- or interstitial-related point defects are particularly effective in impeding phonon transport since they induce substantial lattice distortion.[52–59] Therefore, we consider the remarkable reduction of κ_L has an origin of point defect scattering in which the vacancy sites are involved.

2.3.2 Calculation of the defect formation enthalpy. To clarify the specific atom that occupies the 4d position, we employ first-principle calculations to evaluate the formation enthalpy (H_f) of different defects. Herein, we consider three types of defects: the interstitial defects, the vacancy defects, and the Frenkel defects. To be specific, a Frenkel defect, for example, the Zr/4d, is defined as one Zr atom occupying the interstitial 4d position (I_{Zr}) and leaving one void at the original Zr position (V_{Zr}). Therefore, the formation enthalpy of Zr/4d Frankel defect can be approximated as the summation of the formation enthalpies of I_{Zr} and V_{Zr}. Fig. 9a and b show the Fermi-level (μ_e) dependent H_f of interstitials (I_{Zr}, I_{Co}, I_{Sb}) and vacancies (V_{Zr}, V_{Co}, V_{Sb}), respectively. We find that, in the vicinity of the valence band, the Co atoms consume lower energy than the Zr and Sb atoms for the formation of both interstitials (Fig. 9a) and vacancies (Fig. 9b). Besides, we evaluate the H_f of Frenkel defects (Zr/4d, Co/4d, and Sb/4d) directly. Interestingly, only the Co/4d defect is calculable, and its H_f is presented in Fig. 9c. Neither the Zr/4d nor Sb/4d Frenkel defects are thermodynamically stable. Overall, these results support the involvement of Co atoms in occupying the Wyckoff 4d position of half-Heulser compounds $ZrCoSb_{1-x}Sn_x$.

Our calculations have shown that the I_{Co} (+2) and the V_{Co} (+1) defects are the lowest-energy states, and independently they should sum up to +3 charge state in total. This is also following the prediction using Zintl chemistry.[60,61] On the other hand, when the two types of defects are close to each other, such as in the same supercell when calculating the Co/4d Frenkel defects, the summed charge of I_{Co} and V_{Co} differs from the charge of Co/4d (+2) near the vicinity of the valence band, as shown in Fig. 9c. This is because confining the vacancies and interstitials in the same supercell yields unphysical interactions in between. In reality, the charge state of +3 should be expected for Co/4d, since the independent I_{Co} and V_{Co} defects tend to repel each other due to the Coulomb interaction.

2.3.3 Stoichiometry determination based on EDX and ICP. Although we confirm the involvement of Co atoms in the occupation of 4d lattice sites, it remains obscure whether the Co atoms at the 4d lattice sites are migrated from the 4c sites (Frenkel defects) or excessively included into the interstitial sites (like $ZrNi_{1+\delta}Sn$). Therefore, we investigate the stoichiometry of the ZrCoSb-based compounds by employing SEM-EDX combining an inductively coupled plasma mass spectrometry (ICP) of which the details are shown in the ESI† (Tables S2, S3 and Fig. S13). We show in Table 2 the EDX and ICP stoichiometry of the compounds ZrCoSb, $ZrCoSb_{0.8}Sn_{0.2}$, and $Zr_{0.8}Ti_{0.2}$-CoSb. Both techniques yield elemental quantities that are very close to the nominal composition, suggesting that the concentration of excessive interstitial Co (I_{Co}), if any, should not exceed 1% even after including the measurement errors from EDX and ICP deliberately. Evidently, the ZrCoSb-based compounds differ from the ZrNiSn-based ones in the way of occupying the 4d lattice sites, and the presence of Frenkel-type point defects in the lattice is supported.

2.3.4 Rietveld refinement to quantify the defect concentration. Subsequently, we employ Rietveld refinement to quantify the amount of Co/4d defects for compounds ZrCoSb, $Zr_{0.8}Ti_{0.2}CoSb$, $ZrCoSb_{0.8}Sn_{0.2}$ and $ZrCoSb_{0.7}Sn_{0.3}$. For each of

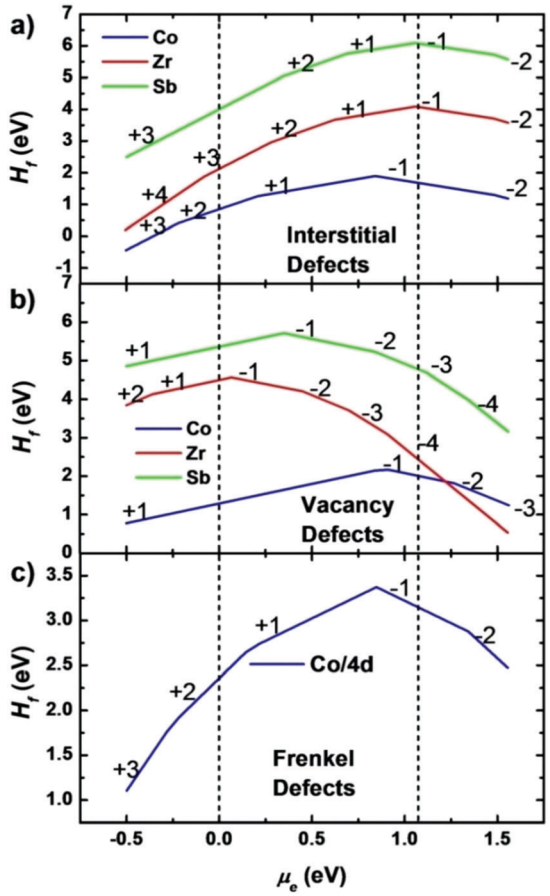

Fig. 9 The chemical-potential-dependent formation enthalpy (H_f) of (a) interstitial defects, (b) vacancy defects, and (c) Frenkel defects of Zr, Co, and Sb atoms. Note that for Frenkel defects, only Co/4d is thermodynamically stable. The numbers alongside the lines are the charging states of the defects at the corresponding chemical potentials. The zero value of chemical potential represents the valence band maximum, and the dashed vertical lines define the bandgap.

Table 2 The EDX- and ICP-compositions of $ZrCoSb_{0.8}Sn_{0.2}$, ZrCoSb, and $Zr_{0.8}Ti_{0.2}CoSb$. The content of Co atoms is set as unity

Nominal composition	EDX composition	ICP composition
$ZrCoSb_{0.8}Sn_{0.2}$	$Zr_{1.01}CoSb_{0.79}Sn_{0.18}$	$Zr_{1.017}CoSb_{0.799}Sn_{0.199}$
ZrCoSb	$Zr_{1.02}CoSb_{0.99}$	$Zr_{1.010}CoSb_{1.015}$
$Zr_{0.8}Ti_{0.2}CoSb$	$Zr_{0.81}Ti_{0.21}CoSb_{0.98}$	$Zr_{0.811}Ti_{0.201}CoSb_{1.011}$

them, we compare the refinements with assumptions of a perfect crystal (no defect) or Frenkel defects (Co/4d). The latter allows a flexible migration of Co atoms between the 4c $(\frac{1}{4}, \frac{1}{4}, \frac{1}{4})$ and the 4d $(\frac{3}{4}, \frac{3}{4}, \frac{3}{4})$ sites with the constraint that the total occupancy for both Co sites is 100%. The refinement patterns are compared in the ESI,† with or without the Co/4d defects (Fig. S14). Table 3 shows that high-quality refinements are realized for the compounds even when no defects are considered, suggesting that the specimens are highly ordered already and the defect concentration is small. Nevertheless, the refinement qualities still improve slightly upon including ~1.06% and ~1.92% Co/4d Frenkel defects for $ZrCoSb_{0.8}Sn_{0.2}$ and $ZrCoSb_{0.7}Sn_{0.3}$, respectively, as confirmed by the consistently reduced refinement parameters (Chi2, R-factor, RF-factor) from Table 3. A similar refinement was performed for NbFeSb to quantify the Fe/4d Frenkel defects.[62] On the other hand, refining the Sn-free compounds ($Zr_{0.8}Ti_{0.2}CoSb$ and ZrCoSb) ends up with physically meaningless results (negative occupation at the 4d sites) if the Co/4d defects are permitted. Therefore, the point-defect feature of the Sn-containing compounds is essentially different from the Sn-free ones. Furthermore, since the κ_L is weakly related to the synthesis and the impurity features of ZrCoSb, as shown in the ESI† (Section 2.2.2), we anticipate the formation of Co/4d defects are induced by a charge-compensation effect that also significantly impact the electronic transport properties, as briefly discusses in the ESI.† As confirmed by Fig. 9, the positively charged Co/4d defects in the vicinity of the valence band show their donor-like nature, which is indeed favored by the charge-compensation effect under p-type doping.

2.3.5 Phonon scattering from Co/4d Frenkel defects. Ultimately, we employ the BvK–Debye model to analyze the impact of Co/4d Frenkel defects in the κ_L reduction.[63] The calculation details can be found in the ESI† (Section XIII). Fig. 10 shows the calculated concentrations of the Co/4d Frenkel defects being 2.5% and 3.3% for $ZrCoSb_{0.8}Sn_{0.2}$ and $ZrCoSb_{0.7}Sn_{0.3}$, respectively. Besides, we estimate similar defect concentrations (~2.2% and ~2.9%) using another approach by considering the charge-compensation effect, as discussed in the ESI† (Section XIV and Fig. S16). These values slightly differ from the Rietveld refinement results (1.06% and 1.92%, as shown in Table 3), probably due to the uncertainties in the refinement. Nevertheless, the defect concentration calculated from the BvK–Debye model matches the refinement results satisfactorily, which further supporting the origin of the anomalous reduction of κ_L in ZrCoSb being an intensified Co/4d Frenkel point defects scattering upon the substitution of Sn at the Sb sites. The paired defects of vacancies and interstitials, as shown in Fig. 1, not only create considerable mass contrast at

Table 3 Rietveld refinement results of $ZrCoSb_{0.8}Sn_{0.2}$, $ZrCoSb_{0.7}Sn_{0.3}$, ZrCoSb, and $Zr_{0.8}Ti_{0.2}CoSb$ with/without the Co/4d Frenkel defect

	$ZrCoSb_{0.8}Sn_{0.2}$		$ZrCoSb_{0.7}Sn_{0.3}$		ZrCoSb		$Zr_{0.8}Ti_{0.2}CoSb$	
Defects	No defect	Co/4d	No defect	Co/4d	No defect	Co/4d	No defect	Co/4d
Quantity	—	**1.06%**	—	**1.92%**	—	Negative	—	Negative
Chi2	4.9	4.82	3.212	3.106	3.54	—	2.37	—
R-factor	1.81	1.52	2.816	2.21	1.5	—	1.36	—
RF-factor	0.908	0.862	1.29	1.15	0.994	—	0.982	—

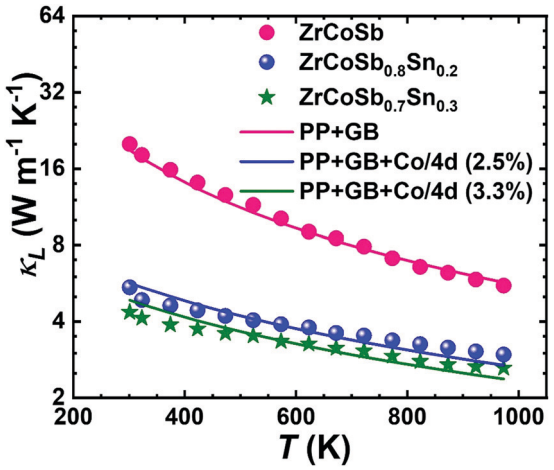

Fig. 10 The experimental lattice thermal conductivity of ZrCoSb, $ZrCoSb_{0.8}Sn_{0.2}$, and $ZrCoSb_{0.7}Sn_{0.3}$, as well as the calculated values based on the BvK–Debye model. Note that the area-weighted grain sizes are obtained from statistical analysis. By considering point defect concentrations of 2.5% and 3.3%, the calculated lattice thermal conductivities agree with the experiments satisfactorily.

the corresponding lattice sites but also greatly alter the bonding configurations inside the lattice by simultaneously breaking existing bonds and forming new bonds. In combination, these effects generate significant lattice distortion, which intensifies phonon scattering and drastically reduces the lattice thermal conductivity.

3 Summary and conclusions

To explain the anomalously reduced κ_L of ZrCoSb when substituting Sn at the Sb sites, we dissociate the individual phonon scattering mechanisms and study their impacts in scattering phonon. Our analyses evidently show that the replacement of Sn only slightly alters the intensity of phonon–phonon interaction. Besides, we exclude the contributions from various mechanisms that can significantly reduce κ_L including phase boundary scattering, grain boundary scattering, and electron–phonon interaction. Subsequently, through a combination of theoretical and experimental approaches, we reveal the existence of Co/4d Frenkel point defects in the Sn-containing ZrCoSb. The formation of donor-like Co/4d defects is electron driven, following the charge-compensation effect upon p-type doping. Subsequently, the defect concentrations are quantified by the Rietveld refinement, which matches well with the calculated ones by considering the BvK–Debye model and the reduced doping efficiency. Our work elucidates the mechanism of increased phonon scattering in half-Heusler compounds ZrCoSb upon substituting Sn at the Sb sites. Last but not least, although these analyses are based on ZrCoSb, we show that our conclusions are extendable to many other half-Heusler compounds such as NbFeSb, ZrNiSn, and ZrCoBi. Our work discloses the necessity for an advanced understanding of the phonon transport for half-Heusler compounds, which is imperative to enable subsequent material optimization and advance their thermoelectric performance.

Author contributions

R. H., K. N., and G. S. designed the research; R. H. and Z. L. performed research; T. Z. and J. C. G. conducted the first-principle calculations; Y. W., U. W., P. P., and D. W. conducted the TEM characterization; L. F. conducted the SEM characterization; J. C. J. and P. Y. performed Rietveld refinement; A. S. measured the sound velocity; NPR conducted the Hall measurement; P. Y., M. W., and G. J. S. contributed analytical tools; R. H., G. S., and K. N. prepared the manuscript; and everyone commented on the manuscript.

Conflicts of interest

The authors declare no conflict of interest.

Acknowledgements

Various computational resources are used in this work: (i) Comet at the Extreme Science and Engineering Discovery Environment (XSEDE), which is supported by National Science Foundation grant number ACI-1548562, through allocation TG-DMR090027, and (ii) the National Energy Research Scientific Computing Center (NERSC), which is supported by the Office of Science of the U.S. Department of Energy under Contract No. DE-AC02-05CH11231. ZL acknowledges financial support from the China Scholarship Council (CSC) under the Grant CSC Nr. 201806080011. PP acknowledges financial support from the Deutsche Forschungsgemeinschaft (DFG LU 2261/6-1). Thanks to Dr Bonny Dongre and Dr Georg Madsen at the TU Wien for the inspiring discussions. Thanks to Ms Andrea Voss for her support on the ICP measurement. Thanks to Ms Juliane Scheiter for her support on the Hall measurement.

References

1 G. Li, J. Garcia Fernandez, D. A. Lara Ramos, V. Barati, N. Pérez, I. Soldatov, H. Reith, G. Schierning and K. Nielsch, *Nat. Elect.*, 2018, **1**, 555–561.
2 D. Narducci, *JPhys Energy*, 2019, **1**, 024001.
3 C. B. Vining, *Nat. Mater.*, 2009, **8**, 83–85.
4 T. Zhu, Y. Liu, C. Fu, J. P. Heremans, J. G. Snyder and X. Zhao, *Adv. Mater.*, 2017, **29**, 1605884.
5 S. Chen and Z. Ren, *Mater. Today*, 2013, **16**, 387–395.
6 C. Fu, S. Bai, Y. Liu, Y. Tang, L. Chen, X. Zhao and T. Zhu, *Nat. Commun.*, 2015, **6**, 9144.
7 H. Zhu, R. He, J. Mao, Q. Zhu, C. Li, J. Sun, W. Ren, Y. Wang, Z. Liu, Z. Tang, A. Sotnikov, Z. Wang, D. Broido, D. J. Singh, G. Chen, K. Nielsch and Z. Ren, *Nat. Commun.*, 2018, **9**, 2497.
8 J. Yu, C. Fu, Y. Liu, K. Xia, U. Aydemir, T. C. Chasapis, G. J. Snyder, X. Zhao and T. Zhu, *Adv. Energy Mater.*, 2018, **8**, 1701313.
9 G. Rogl, P. Sauerschnig, Z. Rykavets, V. V. Romaka, P. Heinrich, B. Hinterleitner, A. Grytsiv, E. Bauer and P. Rogl, *Acta Mater.*, 2017, **131**, 336–348.
10 L. Chen, Y. Liu, J. He, T. M. Tritt and S. J. Poon, *AIP Adv.*, 2017, **7**, 065208.

11 G. Rogl, A. Grytsiv, M. Gürth, A. Tavassoli, C. Ebner, A. Wünschek, S. Puchegger, V. Soprunyuk, W. Schranz, E. Bauer, H. Müller, M. Zehetbauer and P. Rogl, *Acta Mater.*, 2016, **107**, 178–195.
12 R. He, S. Gahlawat, C. Guo, S. Chen, T. Dahal, H. Zhang, W. Liu, Q. Zhang, E. Chere, K. White and Z. Ren, *Phys. Status Solidi A*, 2015, **212**, 2191–2195.
13 W. Xie, A. Weidenkaff, X. Tang, Q. Zhang, J. Poon and T. Tritt, *Nanomaterials*, 2012, **2**, 379–412.
14 L.-D. Zhao, S.-H. Lo, Y. Zhang, H. Sun, G. Tan, C. Uher, C. Wolverton, V. P. Dravid and M. G. Kanatzidis, *Nature*, 2014, **508**, 373–377.
15 B. Poudel, Q. Hao, Y. Ma, Y. Lan, A. Minnich, B. Yu, X. Yan, D. Wang, A. Muto, D. Vashaee, X. Chen, J. Liu, M. S. Dresselhaus, G. Chen and Z. Ren, *Science*, 2008, **320**, 634–638.
16 E. Rausch, B. Balke, S. Ouardi and C. Felser, *Phys. Chem. Chem. Phys.*, 2014, **16**, 25258–25262.
17 X. Yan, G. Joshi, W. Liu, Y. Lan, H. Wang, S. Lee, J. W. Simonson, S. J. Poon, T. M. Tritt, G. Chen and Z. F. Ren, *Nano Lett.*, 2011, **11**, 556–560.
18 R. He, D. Kraemer, J. Mao, L. Zeng, Q. Jie, Y. Lan, C. Li, J. Shuai, H. S. Kim, Y. Liu, D. Broido, C.-W. Chu, G. Chen and Z. Ren, *Proc. Natl. Acad. Sci. U. S. A.*, 2016, **113**, 13576–13581.
19 H. Xie, H. Wang, Y. Pei, C. Fu, X. Liu, G. J. Snyder, X. Zhao and T. Zhu, *Adv. Funct. Mater.*, 2013, **23**, 5123–5130.
20 C. Fu, H. Wu, Y. Liu, J. He, X. Zhao and T. Zhu, *Adv. Sci.*, 2016, **3**, 1600035.
21 J. M. Ziman, *Philos. Mag.*, 1956, **1**, 191–198.
22 A. B. Pippard, *The London, Edinburgh, and Dublin Philosophical Magazine and Journal of Science*, 2010, **46**, 1104–1114.
23 R. He, H. Zhu, J. Sun, J. Mao, H. Reith, S. Chen, G. Schierning, K. Nielsch and Z. Ren, *Mater. Today Phys.*, 2017, **1**, 24–30.
24 R. He, L. Huang, Y. Wang, G. Samsonidze, B. Kozinsky, Q. Zhang and Z. Ren, *APL Mater.*, 2016, **4**, 104804.
25 T. Wu, W. Jiang, X. Li, Y. Zhou and L. Chen, *J. Appl. Phys.*, 2007, **102**, 103705.
26 E. S. Toberer, A. Zevalkink and G. J. Snyder, *J. Mater. Chem.*, 2011, **21**, 15843.
27 C. Chang and L.-D. Zhao, *Mater. Today Phys.*, 2018, **4**, 50–57.
28 K. Wang, P. F. Luo, L. Liu, J. J. Xing, Y. Jiang, J. Luo and H. Gu, *Mater. Today Phys.*, 2019, **11**, 100173.
29 J. P. A. Makongo, D. K. Misra, X. Zhou, A. Pant, M. R. Shabetai, X. Su, C. Uher, K. L. Stokes and P. F. P. Poudeu, *J. Am. Chem. Soc.*, 2011, **133**, 18843–18852.
30 N. S. Chauhan, S. Bathula, B. Gahtori, Y. V. Kolen'ko, R. Shyam, N. K. Upadhyay and A. Dhar, *J. Appl. Phys.*, 2019, **126**, 125110.
31 G. Joshi, X. Yan, H. Wang, W. Liu, G. Chen and Z. Ren, *Adv. Energy Mater.*, 2011, **1**, 643–647.
32 C. Yu, H. Xie, C. Fu, T. Zhu and X. Zhao, *J. Mater. Res.*, 2012, **27**, 2457–2465.
33 R. He, H. S. Kim, Y. Lan, D. Wang, S. Chen and Z. Ren, *RSC Adv.*, 2014, **4**, 64711–64716.
34 C. Hu, K. Xia, X. Chen, X. Zhao and T. Zhu, *Mater. Today Phys.*, 2018, **7**, 69–76.
35 Z. Tian, K. Esfarjani, J. Shiomi, A. S. Henry and G. Chen, *Appl. Phys. Lett.*, 2011, **99**, 053122.
36 M. Zebarjadi, K. Esfarjani, M. S. Dresselhaus, Z. F. Ren and G. Chen, *Energy Environ. Sci.*, 2012, **5**, 5147–5162.
37 J. Zhou, H. Zhu, T.-H. Liu, Q. Song, R. He, J. Mao, Z. Liu, W. Ren, B. Liao, D. J. Singh, Z. Ren and G. Chen, *Nat. Commun.*, 2018, **9**, 1721.
38 S. N. H. Eliassen, A. Katre, G. K. H. Madsen, C. Persson, O. M. Løvvik and K. Berland, *Phys. Rev. B: Condens. Matter Mater. Phys.*, 2017, **95**, 045202.
39 B. Liao, B. Qiu, J. Zhou, S. Huberman, K. Esfarjani and G. Chen, *Phys. Rev. Lett.*, 2015, **114**, 115901.
40 Q. Xu, J. Zhou, T.-H. Liu and G. Chen, *Appl. Phys. Lett.*, 2019, **115**, 023903.
41 B. Dongre, J. Carrete, S. Wen, J. Ma, W. Li, N. Mingo and G. K. H. Madsen, *J. Mater. Chem. A*, 2020, **8**, 1273–1278.
42 Q. Ren, C. Fu, Q. Qiu, S. Dai, Z. Liu, T. Masuda, S. Asai, M. Hagihala, S. Lee, S. Torri, T. Kamiyama, L. He, X. Tong, C. Felser, D. J. Singh, T. Zhu, J. Yang and J. Ma, *Nat. Commun.*, 2020, **11**, 3142.
43 P. G. Klemens, *Phys. Rev.*, 1960, **119**, 507–509.
44 J. Callaway, *Phys. Rev.*, 1959, **113**, 1046–1051.
45 J. Callaway and H. C. von Baeyer, *Phys. Rev.*, 1960, **120**, 1149–1154.
46 M. Zhou, C. Feng, L. Chen and X. Huang, *J. Alloys Compd.*, 2005, **391**, 194–197.
47 H.-H. Xie, J.-L. Mi, L.-P. Hu, N. Lock, M. Chirstensen, C.-G. Fu, B. B. Iversen, X.-B. Zhao and T.-J. Zhu, *CrystEngComm*, 2012, **14**, 4467.
48 H. Xie, H. Wang, C. Fu, Y. Liu, G. J. Snyder, X. Zhao and T. Zhu, *Sci. Rep.*, 2014, **4**, 6888.
49 R. A. Downie, S. A. Barczak, R. I. Smith and J. W. G. Bos, *J. Mater. Chem. C*, 2015, **3**, 10534–10542.
50 V. A. Romaka, P. Rogl, V. V. Romaka, Y. V. Stadnyk, E. K. Hlil, V. Y. Krajovskii and A. M. Horyn, *Semiconductors*, 2013, **47**, 892–898.
51 R. Akram, Q. Zhang, D. Yang, Y. Zheng, Y. Yan, X. Su and X. Tang, *J. Electron. Mater.*, 2015, **44**, 3563–3570.
52 Y. Pei and D. T. Morelli, *Appl. Phys. Lett.*, 2009, **94**, 122112.
53 Y. Lee, S. Lee and G. S. Hwang, *Phys. Rev. B: Condens. Matter Mater. Phys.*, 2011, **83**, 125202.
54 Z. Qu, T. D. Sparks, W. Pan and D. R. Clarke, *Acta Mater.*, 2011, **59**, 3841–3850.
55 J. Mao, J. L. Niedziela, Y. Wang, Y. Xia, B. Ge, Z. Liu, J. Zhou, Z. Ren, W. Liu, M. K. Y. Chan, G. Chen, O. Delaire, Q. Zhang and Z. Ren, *Nano Energy*, 2018, **48**, 189–196.
56 A. Zevalkink, W. G. Zeier, E. Cheng, J. Snyder, J.-P. Fleurial and S. Bux, *Chem. Mater.*, 2014, **26**, 5710–5717.
57 Z. Li, C. Xiao, S. Fan, Y. Deng, W. Zhang, B. Ye and Y. Xie, *J. Am. Chem. Soc.*, 2015, **137**, 6587–6593.
58 R. Guo and S. Lee, *Mater. Today Phys.*, 2020, **12**, 100177.
59 T. Fang, K. Xia, P. Nan, B. Ge, X. Zhao and T. Zhu, *Mater. Today Phys.*, 2020, **13**, 100200.

60 S. Anand, K. Xia, V. I. Hegde, U. Aydemir, V. Kocevski, T. Zhu, C. Wolverton and G. J. Snyder, *Energy Environ. Sci.*, 2018, **11**, 1480–1488.
61 W. G. Zeier, J. Schmitt, G. Hautier, U. Aydemir, Z. M. Gibbs, C. Felser and G. J. Snyder, *Nat. Rev. Mater.*, 2016, **1**, 16032.
62 D. Hobbis, R. P. Hermann, H. Wang, D. S. Parker, T. Pandey, J. Martin, K. Page and G. S. Nolas, *Inorg. Chem.*, 2019, **58**, 1826–1833.
63 R. Gurunathan, R. Hanus and G. J. Snyder, *Mater. Horiz.*, 2020, **7**, 1452–1456, DOI: 10.1039/c9mh01990a.